ADVANCED MATERIALS INTERFACES
Open Access
www.advmatinterfaces.de

Sol–Gel Thin Films for the Protection of Ancient Glass Artifacts: A Performance Comparison Between Inorganic and Hybrid Silica Compositions

Stefano Centenaro, Elti Cattaruzza, Antonella Glisenti, Leonardo Puppulin, Giulia Franceschin, and Arianna Traviglia**

The preservation of archaeological and historical glass requires advanced conservation strategies. While some existing methods are effective in some instances, they often have limitations, such as the need for high-temperature densification treatments or undesirable interactions with the glass substrate. This study investigates the development of sol–gel-based protective coatings for glass, focusing on both inorganic and hybrid formulations. The main aim is to formulate silica sol–gel solutions catalyzed with low acid concentrations and applied at room temperature, reducing the risks associated with conventional methods while enhancing the long-term preservation of ancient artifacts. Silica-based coatings are synthesized using three silica precursors–one fully inorganic and two containing organic alkyl groups of different lengths–along with variations in the molar ratio of precursors, water and ethanol. These formulations are applied to soda-lime glass substrates via dip coating, forming thin films between 100 and 150 nm. The coated samples undergo multiscale analysis, including accelerated ageing tests to simulate environmental degradation. Results demonstrate that hybrid coatings functionalized with methyl and octyl groups provide superior barriers against the diffusion of alkaline and alkaline-earth elements, outperforming purely inorganic coatings. This research highlights the potential of hybrid sol–gel coatings as effective and durable protective solutions for glass conservation.

1. Introduction

Ancient glass objects, exposed to environmental moisture, temperature fluctuations and pollutants over centuries, often suffer from various forms of alteration, such as leaching, loss of transparency, iridescence and cracking (*crizzling*).[1] The ongoing discussion in this field emphasizes the importance of effective yet sustainable conservation techniques, highlighting the need to refine and expand traditional approaches. While some existing methods are effective in some instances, their practical application is often limited by the need for high-temperature treatments to densify coatings or by unfavorable interactions with glass substrates that may accelerate degradation.

This work aims to develop and evaluate sol–gel-based protective coatings for glass, using both inorganic and hybrid formulations. The goal is to create silica sol–gel solutions catalyzed with a low concentration of acid and deposited at room temperature, reducing the risks of current formulations while enhancing the long-term preservation of ancient artifacts.

Sol–gel technology has been extensively studied in the field of conservation, offering a promising approach for developing durable protective coatings that can help maintain the integrity and aesthetic qualities of glass artifacts. This technique facilitates the preparation of both inorganic and hybrid materials.[2] The use of tetraethyl orthosilicate (TEOS) as a precursor in sol–gel formulations has been widely tested. Acid-catalyzed TEOS-based solutions have proven effective in depositing protective coatings on soda-lime silicate glass,[3,4] demonstrating good transparency and mechanical strength without requiring high temperature treatments.

However, several limitations have emerged in the application of these coating to ancient glass. The acidic nature of sol–gel formulations can induce ion leaching from the glass substrate, potentially weakening the coating and accelerating the degradation of glass itself.[5] This issue is especially problematic for chemically unstable glass, such as that in ancient artifacts, where even minor alterations can lead to significant deterioration.

S. Centenaro, G. Franceschin, A. Traviglia
Center for Cultural Heritage Technologies (CCHT)
Istituto Italiano di Tecnologia (IIT)
Epsilon building, via Torino 155, Venezia-Mestre 30170, Italia
E-mail: giulia.franceschin@iit.it; arianna.traviglia@iit.it

S. Centenaro, E. Cattaruzza, L. Puppulin
Dipartimento di Scienze Molecolari e Nanosistemi (DSMN)
Università Ca' Foscari Venezia
Eta Building, via Torino 155, Venezia-Mestre 30170, Italia

A. Glisenti
Dipartimento di Scienze Chimiche (DiSC)
Università degli Studi di Padova
via Marzolo 1, Padova 35131, Italia

The ORCID identification number(s) for the author(s) of this article can be found under https://doi.org/10.1002/admi.202500061

DOI: 10.1002/admi.202500061

Table 1. Overview of the abbreviations for the studied samples, including the silica precursor type, name and chemical formula used in their preparation.

	Silica precursor type	Silica precursor name	Silica precursor chemical formula
SGT	Inorganic	TEOS	$Si(OC_2H_5)_4$
SGTM	Methyl-modified	MTES	$CH_3Si(OC_2H_5)_3$
SGTO	Octyl-modified	OTES	$C_8H_{17}Si(OC_2H_5)_3$

Previous research has explored various strategies to mitigate these effects, including the use of alternative catalysts like Pb^{2+}. While Pb^{2+}-catalyzed TEOS coatings have shown promise, particularly in forming transparent films on lead-silicate glass, they have led to undesirable side effects such as iridescence and color changes due to lead ion diffusion.[6]

The need for low-temperature application methods has also driven the exploration of organically modified silica alkoxides,[7] which combine the benefits of organic flexibility with inorganic durability. Such hybrid formulations provide coatings with improved mechanical properties, such as enhanced elasticity and hydrophobicity, making them suitable for outdoor applications where exposure to moisture and pollutants is common. Commercial products like SIOX-5 have been successfully applied in the restoration of stained-glass windows, showing excellent initial performance in preventing water ingress and preserving the aesthetic qualities of glass surfaces.[8] However, the long-term stability of these coatings on aged glass artifacts remains under investigation, particularly concerning their interaction with unstable substrates.

Other studies have explored modifications to the sol–gel process to overcome the challenges of glass artifact preservation. For example, Carmona et al. examined hybrid coatings based on TEOS and organically modified silanes such as 3-trimethoxysilyl propyl methacrylate. Their research[9] found that hybrid formulations could extend the pot life and enhance adhesion, making them more suitable for the consolidation of delicate, unstable glass surfaces. Despite promising results on replica samples, further testing on actual historical glass artifacts is needed to ensure that these coatings are both effective and reversible in real-world applications.

Recent developments also include the use of perhydropolysilazane (PHPS)-derived coatings, which, through conversion to silica at relatively low temperatures, offer a potentially less aggressive approach to glass protection. Palladium and ammonia vapors were used to catalyze the conversion of PHPS to silica,[10] offering protective coatings with high transparency and stability. However, challenges remain in controlling the efficiency of the conversion process and managing the migration of mobile ions from the soda-lime glass substrate, which can undermine the coating's long-term performance.[11]

These existing sol–gel formulations, while offering substantial progress, present several challenges that have yet to be fully addressed. Many formulations either require high temperatures for film densification, are too acidic for fragile substrates, or have long-term stability issues that affect their suitability for historical glass conservation. The need for coatings that can be applied at room temperature, are minimally invasive, and effectively prevent degradation over time remains critical. Therefore, this study aims to further the understanding of sol–gel coatings, focusing on hybrid formulations that combine the benefits of both inorganic and organic components, to provide more effective, stable, and reversible protective coatings for glass artifacts.

The present research is based on the hypothesis that sol–gel coatings synthesized from TEOS and organically modified silanes, such as methyltriethoxysilane (MTES) and octyltriethoxysilane (OTES), can provide enhanced performances compared to previously synthesized inorganic coatings. These hybrid films, prepared and applied at room temperature, are expected to prevent the leaching of alkaline elements, maintain transparency, and offer long-term stability under environmental stress.

To confirm this hypothesis, different sol–gel syntheses, using TEOS, MTES, and OTES as precursors, were prepared, varying the molar ratio of precursors, water and ethanol. These formulations were applied to soda-lime glass substrates via dip coating to form thin films ranging from 100 to 150 nm. The coated samples were submitted to a comprehensive multi-scale analysis, including accelerated ageing tests to simulate environmental degradation. Techniques such as infrared spectroscopy (ATR-IR and SR-IR), X-ray photoelectron spectroscopy (XPS), and atomic force microscopy (AFM) were employed to characterize the physicochemical properties of the coatings and assess their barrier effectiveness against the leaching of sodium and calcium.

2. Results and Discussion

Before assessing the durability of the sol–gel coatings under artificial ageing conditions, their initial physical and chemical properties were assessed. The results from a multi-technique characterization provided insights into the coatings' structure, thickness, and optical properties, which are critical for determining their effectiveness in protecting glass artifacts. **Table 1** summarizes the abbreviations used to refer to the distinct coatings studied. The structural formula of the compounds used as silica precursors is shown in **Figure 1**a.

2.1. Effects of the Sol–Gel Composition on the Coating Characteristics

2.1.1. Effect on Chemical Properties

The Fourier transform infrared (FT-IR) spectroscopy, conducted in both specular reflectance (SR) and attenuated total reflectance (ATR) configurations, provided crucial insights into the chemical structure and functionalities of the coatings, properties that directly influence their physical properties and protective performance.

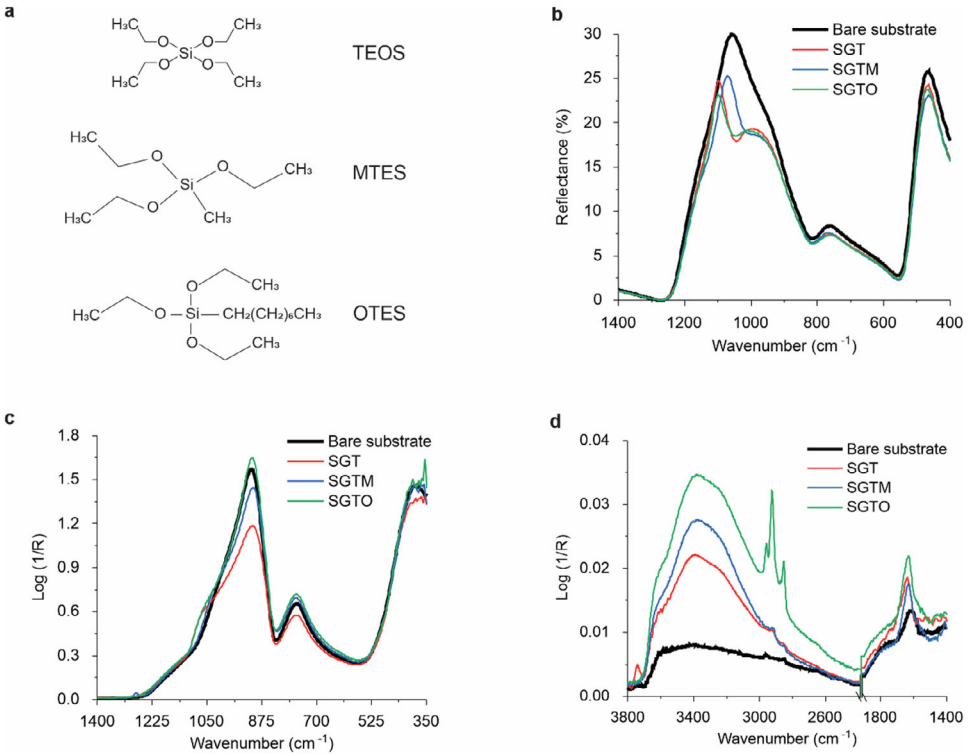

Figure 1. a) Structural formulas of the compounds used as silica precursors; b) Comparison between the as deposited SGTM and SGTO hybrid films with the SGT inorganic coating and the bare glass substrate using SR-IR configuration. c) Comparison between the as deposited SGTM and SGTO hybrid films with the SGT inorganic coating and the bare glass substrate using ATR-IR configuration (low wavenumbers) d) ATR-IR spectra in the range of high wavenumbers.

The SR-IR spectra for both inorganic (SGT) and hybrid (SGTM and SGTO) coatings are shown in Figure 1b and reveal distinct peaks characteristic of silica networks. For the inorganic coating, a prominent peak at 1100 cm^{-1}, attributed to the asymmetric Si—O—Si stretching, is blue-shifted compared to the silica soda-lime glass slide. This shift supports the hypothesis that the coating exhibits a silica-like structure, resembling that of bulk SiO_2 (Figure S4, Supporting Information).

In contrast,the SR-IR spectrum of the SGTO film exhibited a slight broadening of the secondary maximum at ≈1000 cm^{-1}, while the main peak at 1100 cm^{-1} remained unchanged compared to the inorganic SGT coating. This indicates that the incorporation of low concentration of OTES did not alter the silica network significantly. On the other hand, the SGTM spectrum revealed a red shift in the main Si-O-Si vibration peak from 1100 to 1070 cm^{-1}, which is likely due to structural modifications caused by the organic groups in the MTES, such as the formation of larger siloxane rings, higher Si—O—Si bond angles and longer Si—O bond lengths.[12]

Table 2. Comparison of thicknesses between hybrid and inorganic thin films.

	Thickness [nm]
SGT	95±5
SGTM	143±7
SGTO	124±6

The ATR-IR analysis highlighted notable differences in the penetration depth of the IR beam into the coatings compared to SR-IR, especially in the high wavenumber region above 1200 cm^{-1}. The ATR-IR spectra are reported in Figure 1c,d, split into low and high wavenumber ranges. Further detailed analyses comparing the SR-IR and ATR-IR spectra are available as Supplementary Materials. The analyses enabled to evaluate that the penetration depth in ATR-IR was significantly lower by 1–4 orders of magnitude, which emphasizes the surface sensitivity of ATR-IR. In the lower wavenumber region, a shoulder appeared at ≈1050 cm^{-1}, corresponding to the TO mode of the Si-O-Si stretching vibration. Additionally, a significant peak at 1280 cm^{-1}, related to Si—C bond stretching, confirmed the integration of MTES in the methyl-functionalized film (SGTM),[13] while bands at 2955, 2926, and 2856 cm^{-1} confirmed the presence of C-H bond vibrations in the octyl-functionalized film (SGTO),[14,15] reinforcing evidence of the successful integration of organosilanes in the hybrid coatings.

2.2. Effects on Coating Thickness

The introduction of organoalkoxysilanes in the hybrid SGTM and SGTO formulations, prepared and deposited under identical ex-

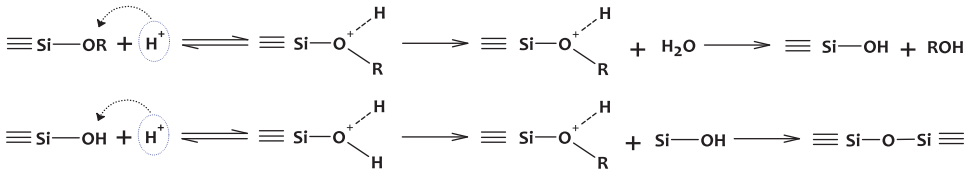

Figure 2. Hydrolysis (top) and condensation (bottom) reaction mechanisms occurring during acid catalysis.

perimental conditions as the inorganic SGT formulation, lead to a significant increase in the thickness of the hybrid films compared to the inorganic one (**Table 2**).

This effect can be attributed to the different reactivities of the precursors. The electron density at the silicon atom depends on the nature of the substituents and decreases in the order shown in Equation (1).[16]

$$\equiv Si - R' > \equiv Si - OR > \equiv Si - OH > \equiv Si - O - Si \quad (1)$$

For acid catalysis, if the electron density at the silicon atom is high, the positive charge of the transition state is stabilized best.[17] Therefore, the reaction rates for hydrolysis and condensation under acidic conditions, illustrated in **Figure 2**, increase in the same order as the electron density.[18] As a consequence, organically substituted alkoxysilanes R'Si(OR)$_3$ have a higher electron density at the silicon atom, reacting faster than the corresponding Si(OR)$_4$ as suggested in Equation (1).

However, the reactivity of organically modified alkoxides also depends on the steric hindrance of the organic substituent groups.[19] Therefore, when comparing the thickness differences between SGTM and SGTO films, the lower thickness of the SGTO film can be attributed to two main factors. First, the lower concentration of OTES in the formulation compared to the concentration of MTES in the SGTM formulation. Second, the different steric hindrance of the alkyl chains in OTES and MTES, with the longer alkyl chain in OTES providing greater steric hindrance

2.3. Effects on Optical Properties

The transparent nature of glass implies that protective measures do not compromise its visual clarity or aesthetic integrity. Therefore, protective coatings should be carefully formulated to provide effective preservation against environmental degradation while maintaining the optical transparency of the glass surface.

Considering the sol–gel deposition, as shown in **Figure 3**, from the visual observation of the glass slide, no structural colors were observed.

From the total reflectance spectra (**Figure 4**), it is possible to see that the glass has a reflectance of nearly 8% constant across the whole visible range (400–700 nm). This is value agrees with the value of reflected light fraction calculated with the Fresnel equation. Detailed calculations are available in the Supplementary Material.

Considering sol–gel coatings, SGTO coatings show remarkable similarities to the spectrum of the inorganic SGT film. This observation suggests that the inclusion of a long alkyl chain does not significantly alter the optical properties of the silica matrix, probably due to the low concentration of the OTES precursor. Similarly, the SGTM film exhibits transmittance and reflectance spectra closely resembling those of the SGT film. The spectrum did not show significant deviations, probably because methyl groups are smaller than octyl groups; therefore, even if present in higher concentration, they do not drastically impact the overall optical properties of the film.

2.4. Assessment of the Ageing Resistance of the Coatings and Comparison of the Different Compositions

After artificial ageing tests, visual observation revealed a clear difference between coated and uncoated glass slides (Figure S7, Supporting Information). The uncoated part developed white spots and a foggy appearance, while the coated section remained clear, demonstrating the protective effect of the sol–gel coating.

Optical microscopy confirmed this, showing (in **Figure 5**) irregular clusters with needle-like substructure on the uncoated part, with the largest clusters measuring ≈100 µm in diameter. In contrast, the coated part did not exhibit these features, indicating the coating ability to prevent surface alterations.

The diffuse reflectance measurements further supported these observations. As illustrated in Figure 5g, the uncoated glass scattered up to 3% of the incident radiation, whereas the coated part exhibited scattering levels like pristine glass, below 0.5% across

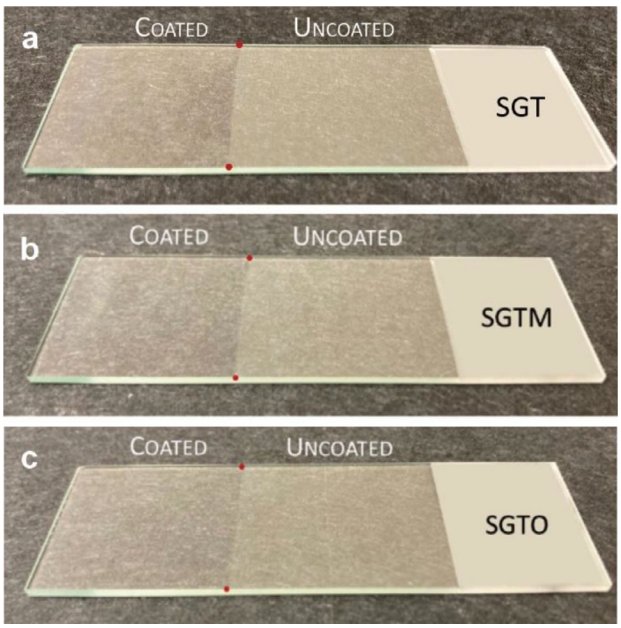

Figure 3. a–c) Photographs of the glass samples SGT, SGTM, and SGTO after applying the formulations via dip coating on half of each substrate.

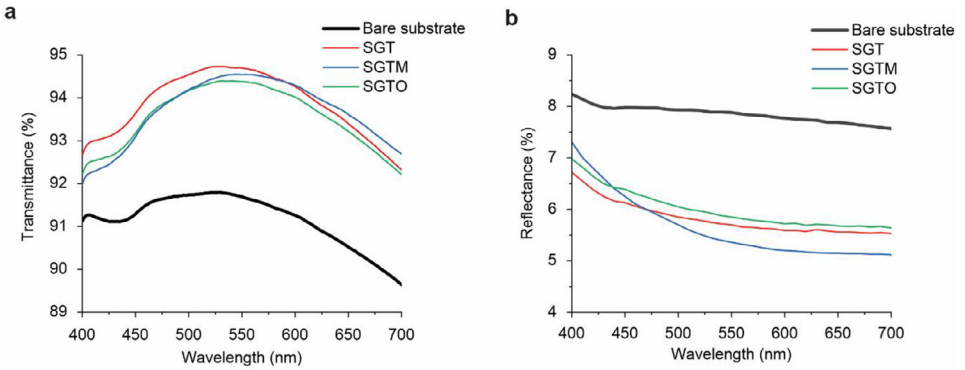

Figure 4. SGTM and SGTO total transmittance spectra a) and total reflectance spectra b) compared to SGT coating and bare glass substrate.

the visible spectrum. This trend was consistent for the hybrid formulations, which exhibited no significant optical differences compared to the inorganic SGT coating. These results showed that the inclusion of organic components did not negatively impact the optical transparency of the coatings after ageing.

The chemical stability of the coating after ageing was confirmed by infrared spectroscopy (both with ATR-IR and SR-IR configurations). For the uncoated glass, changes in the silica fingerprint region, such as the enhancement of the Si-OH shoulder band at 950 cm^{-1} and a reduction in Si—O—Si vibrations in SR-IR spectrum, suggested network disruption and the formation of surface precipitates, likely calcium carbonates. The presence of carbonates was confirmed by a sharp peak at 876 cm^{-1} in the ATR-IR spectrum (**Figure 6**), attributed to calcite, and at 854 cm^{-1} in the SR-IR spectrum, linked to aragonite.[20]

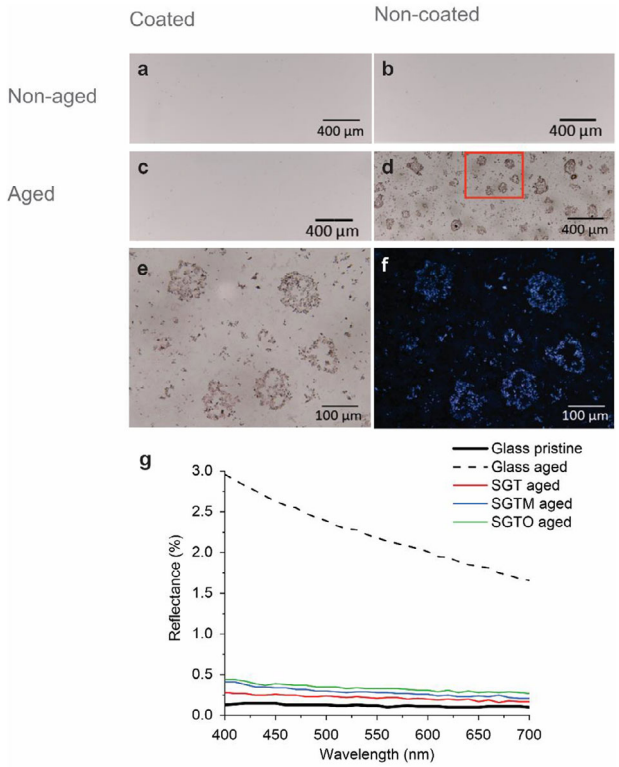

Figure 5. Optical microscopy images in transmitted brightfield configuration of a glass sample before ageing (a is the coated side and b the uncoated side) and after artificial ageing (c is the coated side and d the uncoated side). Detail of optical microscopy images in transmitted brightfield configuration (e) and reflected darkfield configuration (f) of the uncoated aged glass image d. g) Diffuse reflectance spectra of the aged glass and sol–gel coatings compared to pristine glass.

In the high wavenumber region of the ATR-IR spectrum, the band between 1350 and 1550 cm^{-1}, assigned to antisymmetric vibrations (ν_3) of carbonates CO_3^{2-},[21] further confirmed the presence of calcium carbonates. Additionally, a broad band ranging from 2500 to 3700 cm^{-1} was detected after ageing and could be attributed to OH stretching vibrations of Si—OH and H_2O species. These vibrations, associated with varying degrees of hydrogen bonding[22] signal the presence of hydrous species in the subsurface region. While this band provides a qualitative tool for detecting these species, it does not allow for a precise determination of the relative abundance between Si—OH and H_2O species.[23]

On the other hand, the SGT coating showed no significant differences in either the silica fingerprint region at low wavenumbers (Figure 6a,c,e,f) or the OH stretching region at high wavenumbers (Figure 6b,d) after ageing, confirming the chemical stability of the inorganic coating. Similarly, hybrid coatings retained their organic groups even after ageing, with no detectable carbonate signals, indicating their superior resistance to chemical degradation. Additionally, the Si—C bond stretching mode at 1280 cm^{-1} remained unvaried in the SGTM coating's ATR-IR spectrum, while the SGTO coating retained strong C—H stretching bands at 2955, 2926, and 2856 cm^{-1}.

XPS analysis provided complementary information on the surface composition of both uncoated and coated samples before and after ageing, with a sampling depth of ≈10 nm.

XPS analysis confirmed the presence of adventitious carbon contamination on the surface of air-exposed samples, which is common in material surfaces, but does not reflect the true composition of the underlying material. Therefore, only the key constitutive elements were considered in the analysis (i.e., Si, O, Na, and Ca), as detailed in **Table 3** and Supporting Information.

In the uncoated glass, ageing resulted in a significant increase in sodium and calcium concentration in the superficial ageing, indicating the effects of a leaching process. Specifically, calcium concentration on surface increased fivefold compared to the pristine glass. This was coupled with a minor shift in the $Ca2p_{3/2}$

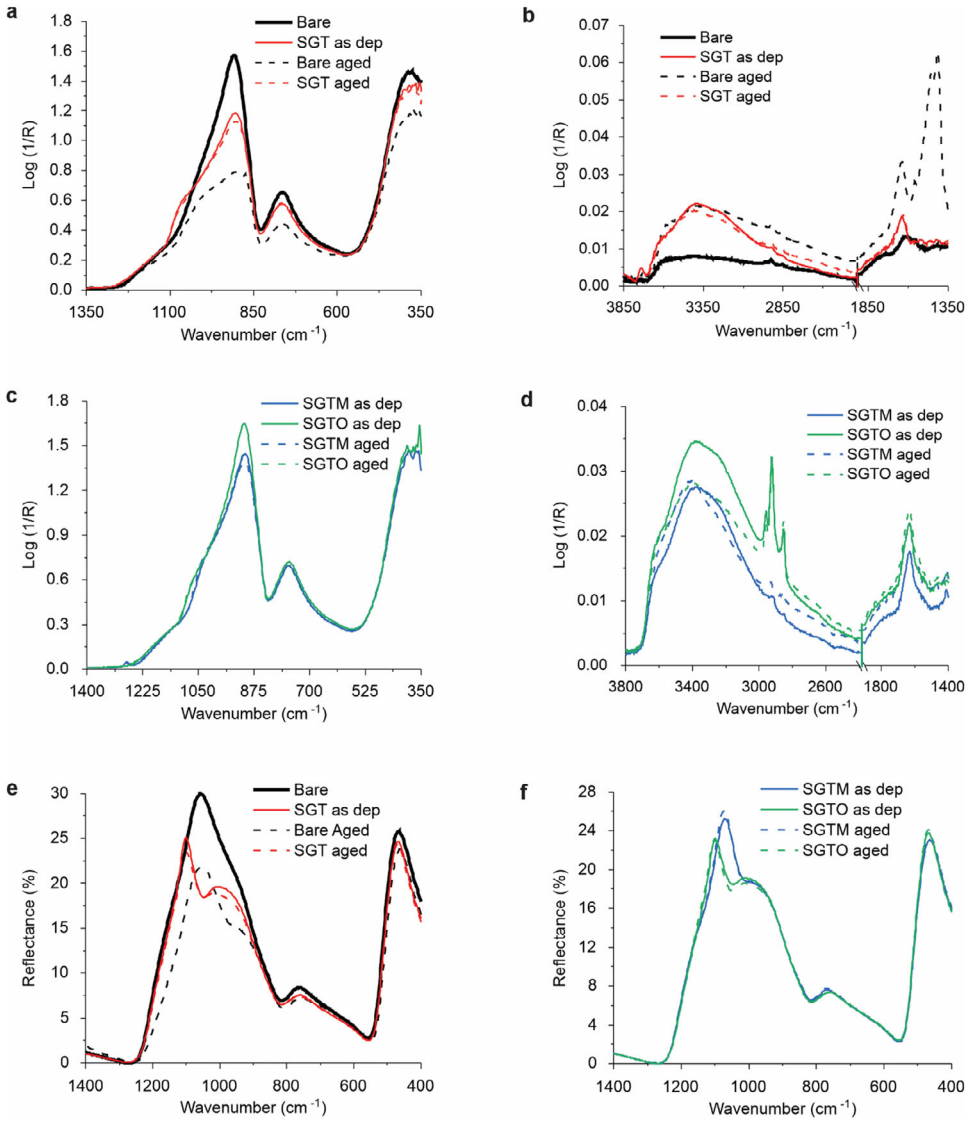

Figure 6. a–d) Comparison between aged glass and SGT aged thin film using ATR-IR configuration e,f) and SR-IR configuration.

binding energy, from 347.1 eV in pristine glass to 347.3 eV post-ageing. Although this shift is within the uncertainty of binding energy measurements, it suggests a potential change in calcium chemical environment, possibly due to the formation of calcium carbonates on the glass surface,[24] thus confirming the IR data analysis.

The formation of carbonates was finally validated by the analysis of the C1s band detected in the aged uncoated glass (**Figure 7**) because, in addition to the main component related to graphitic carbon and derived by adventitious contamination (falling ≈285 eV), a less intense band ≈290 eV is

Table 3. Composition data (in atomic percentage) obtained by XPS analyses on the surface of the uncoated and coated glass before and after artificial ageing tests. Carbon is excluded (see text).

	Glass slide pristine [%at]	Glass slide aged [%at]	SGT aged [%at]	SGTM aged [%at]	SGTO aged [%at]
Si	23.4	12.8	17.2	29.2	28.3
O	67.7	69.4	67.2	67.2	67.3
Na	7.1	8.8	10.0	3.1	4.0
Ca	1.8	9.0	5.6	0.5	0.4

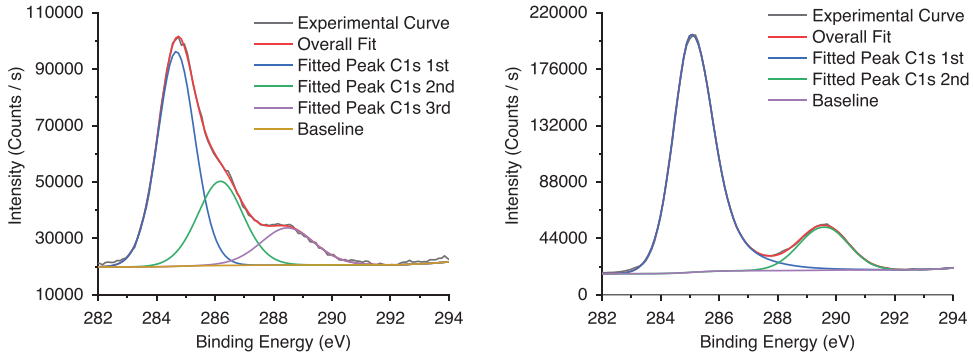

Figure 7. Curve fitting of the XPS spectrum for C1s in the pristine glass (on the left) and aged glass (on the right). The three components detected in the pristine glass are the fingerprint of adventitious carbon contamination.[25]

detected. This last band is consistent with the presence of calcium carbonates.[24]

Sodium also exhibited an increase on the aged glass surface, rising from 7.1% in the pristine sample to 8.8% post-ageing. These compositional changes on the uncoated surface clearly demonstrate the vulnerability of soda-lime-silica glass to environmental degradation, particularly under conditions promoting ion migration. In contrast, the inorganic SGT coating displayed a partial barrier effect, as indicated by the lower concentrations of Ca (5.6%) on the surface after ageing. Although the inorganic sol–gel reduced ion leaching, its barrier capacity was not fully effective, with substantial surface enrichment of Na and Ca still ongoing. On the other hand, the hybrid coating compositions demonstrated superior barrier properties. The SGTM coating showed significantly lower concentrations of Na (3.1%) and Ca (0.5%) after ageing, while the SGTO coating reported similar trends, with Na and Ca concentrations reduced to 4.0% and 0.4%, respectively. These results suggested that the organic modifications in the hybrid coatings effectively enhanced their ability to inhibit the migration of alkaline and alkaline-earth elements.

To further investigate the protective behavior of the studied films, as indicated by XPS results, nano-scale morphological analyses were performed using AFM. Prior to ageing, both the inorganic and hybrid coatings displayed smooth and uniform surfaces, indicating an even distribution of the coating material without significant defects or irregularities. A comparison of the surface morphology and root mean square roughness values between the bare glass and the inorganic coating confirms the coating's homogeneity at the initial state. Detailed results are reported in Figure S8 (Supporting Information). By smoothing surface irregularities, the coating reduces potential sites for moisture and pollutants entrapment, thereby lowering the risk of localized degradation reactions.

After ageing, the inorganic coating SGT exhibited significant changes, developing a cauliflower-like structure composed of nanoparticles ranging from 20 to 40 nm in diameter (Figure S9, Supporting Information). This morphology suggests that the film has undergone densification processes during artificial ageing,[26] which may have led to fissures, serving as pathways for moisture and ion migration.

The superior stability of hybrid formulations was also shown by AFM images, which revealed, particularly for SGTM samples, that the methyl-modified films developed only minor structural rearrangements after ageing. Young's modulus maps in **Figure 8** were calculated using the Derjaguin–Muller–Toporov (DMT) model and confirmed a uniform distribution of organic and inorganic components before ageing, and slight segregation of methyl groups in spherical clusters characterized by a lower value of the elastic modulus compared to the surrounding matrix after ageing. The recorded elastic modulus is consistent with data reported in literature.[27,28] The observed increase in the mean elastic modulus may be attributed to densification processes of the sol–gel film after ageing.

In contrast, the SGTO coating showed more pronounced morphological changes, likely due to the bulkier octyl groups, which led to the formation of elongated oval clusters after ageing, suggesting a separation between the organic and inorganic components of the film (**Figure 9**a,b).

This hypothesis was corroborated by the DMT modulus maps (Figure 9c,d). In the as-deposited state, the maps revealed the interpenetration of two species with distinct elastic moduli, indicating an initially irregular distribution of organic and inorganic components. After artificial ageing tests,

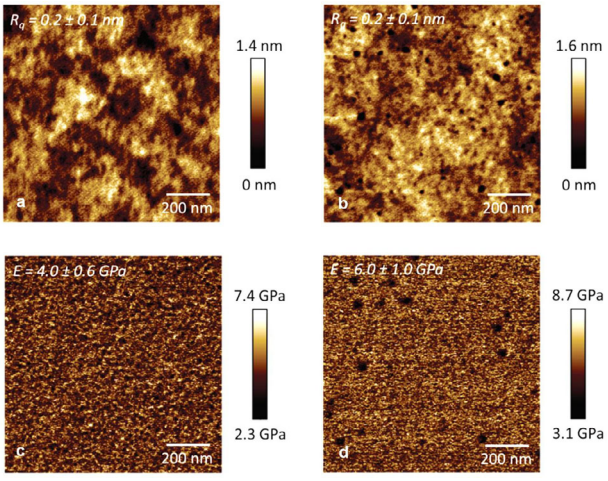

Figure 8. a,b) AFM morphological images of the SGTM coating as deposited and of the SGTM coating after artificial ageing; c,d) AFM DMT modulus images of the SGTM coating as deposited and of the SGTM coating after artificial ageing.

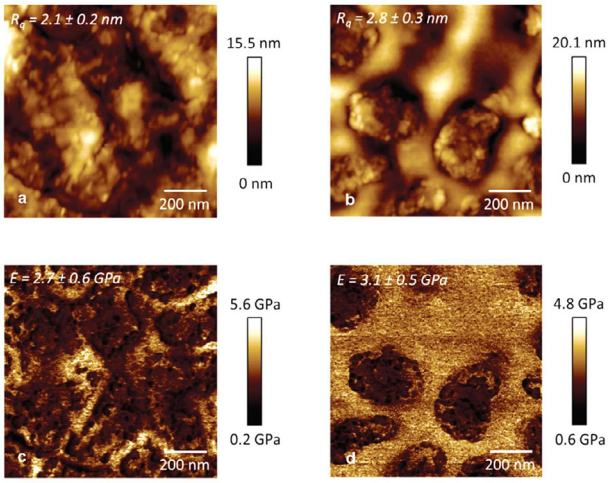

Figure 9. a,b) AFM morphological images of the SGTO coating as deposited and of the SGTO coating after artificial ageing; c,d) AFM DMT modulus images of the SGTO coating as deposited and of the SGTO coating after artificial ageing.

the DMT modulus maps revealed a more ordered structure. This structure was characterized by clusters ≈200 nm in diameter with low elastic modulus values, likely corresponding to the organic component, surrounded by a continuous matrix with higher elastic modulus values, which likely represents the inorganic component. The formation of agglomerates in hybrid films has also been documented in the literature, supporting the observed structural changes in the obtained films.[29,30] Finally, the lower mean value of the elastic modulus might be attributed to the longer alkyl chain incorporated in the SGTO film compared to the methyl groups of the SGTM coating.

The excellent ability of the hybrid coating to prevent ion migration can be better explained by considering how the presence of organic groups in the silica precursors influences the structural and physicochemical properties of the coatings, thereby affecting ion migration across the treated surface. Previous studies have demonstrated that organic functional groups in the silica precursor can enhance cross-linking density and reduce the free volume of the coating network.[31–33] A hybrid silica network promotes the formation of a denser siloxane structure, which significantly improves the barrier properties against ion migration.[29,34,35] Well-structured siloxane networks have been demonstrated to effectively shield the underlying surface by minimizing diffusion pathways and ion transport. Additionally, the presence of organic moieties enhances the coatings' hydrophobicity,[36,37] reducing water contact with the surface – a primary factor in ion migration.[1] These synergistic effects contributed to the superior ion-barrier performances observed in the hybrid compositions studied in this work.

3. Conclusion

This work demonstrated the successful deposition of silica thin films, both inorganic and hybrid, using a sol–gel synthesis with low acid concentrations at room temperature. This approach provided an efficient method for preparing protective coatings for glass surfaces, offering a more accessible and sustainable way for developing high-performance films compared to traditional methods, which typically require more intense acidity and temperature.

The hybrid coatings, functionalized with methyl and octyl groups, exhibited exceptional resistance to ion migration, effectively preventing the diffusion of sodium and calcium ions, which are the primary contributors to the degradation of silica-soda-lime glass. This finding is significant as it tackles the core mechanism behind the deterioration of glass surfaces, demonstrating that the studied coatings enhance the long-term stability and durability of glass, especially in environments where ion interdiffusion is a significant concern.

The coatings also demonstrated remarkable preservation of optical behavior, with UV–vis measurements showing minimal impact on both the transmitted and reflected light. This is a key result, as it proves that the coatings effectively protect the glass without compromising its transparency and aesthetic qualities. This coating feature is particularly important, especially for applications where the visual clarity of glass is critical, such as in glass artifacts conservation. Furthermore, optical microscopy and diffuse reflectance analyses confirmed that the coatings prevented the formation of surface precipitates, unlike uncoated glass, and showed minimal light scattering, which demonstrated the preservation of the pristine appearance of the glass surface.

The durability of the coatings was further confirmed by their performance under artificial ageing conditions. ATR-IR and SR-IR spectroscopy revealed no significant changes in the coatings before and after ageing, indicating that the films maintained their structure and functionality over time. Importantly, there was no evidence of carbonate formation, which is commonly associated with the degradation of glass surfaces. This result emphasized the ability of the studied coatings to withstand environmental and chemical stresses that typically cause surface damage in unprotected glass.

XPS analysis provided additional insights into the coatings' ability to mitigate ion diffusion. While the inorganic films showed partial success in blocking calcium diffusion, they were less effective in preventing sodium migration, likely due to densification and crack formation in the coatings during ageing, as revealed by AFM imaging. In contrast, the hybrid films, functionalized with organic groups, proved to be more effective in blocking both sodium and calcium diffusion. This superior performance highlighted the advantage of hybrid coatings in providing a more comprehensive barrier against ion migration, which is essential for prolonging the durability of glass surfaces in challenging conditions.

These findings underline the potential of hybrid sol–gel coatings as robust and effective protective layers for glass, offering a solution that combines chemical resistance, structural integrity and minimal impact on optical properties. In the field of cultural heritage conservation, these coatings offer an effective means of safeguarding the material without compromising its visual and artistic integrity. Additionally, the practical applications of these coatings extend to industries that require durable, transparent, and chemically resistant glass, paving the way for the development of sustainable, high-performance materials across a wide range of sectors.

Table 4. Overview of the formulation composition for each studied coating, including the molar ratio between the silica precursors and the amount of H_2O, EtOH, and HCl used in the synthesis.

Sample name	Silica precursor mixture ratio	Precursor [mol/L]	H_2O [mol/L]	EtOH [mol/L]	HCl [mol/L]
SGT	TEOS 100%	1	12	20	1.4×10^{-4}
SGTM	TEOS : MTES = 0.55 : 0.45	1	12	20	1.4×10^{-4}
SGTO	TEOS : OTES = 0.95 : 0.05	1	12	20	1.4×10^{-4}

4. Experimental Section

Materials: TEOS (tetraethyl orthosilicate) with purity ≥99%, MTES (triethoxymethylsilane) with purity ≥96%, OTES (triethoxyoctylsilane) with purity ≥96,5%, absolute ethanol (EtOH) with purity ≥99.8%, 2-Propanol (IsoPrOH) with purity ≥99.8%, and hydrochloric acid 37% wt/wt (HCl) were purchased from Sigma–Aldrich and were used as received without further purification. Soda-lime microscope slides with dimensions of 75mm × 27mm × 1.2 mm were purchased from VWR International.

Preparation of Sol–Gel Formulations: The sol precursor was prepared by initially mixing ethanol with Milli-Q water in a 25 mL beaker, using a magnetic stir bar and a digital ceramic hot plate stirrer (Velp Scientifica AREC.X 7). After 5 min, TEOS was added dropwise to the mixture, followed by the dropwise addition of either MTES or OTES (only in the case of the hybrid formulations). Soon after, hydrochloric acid (HCl) was introduced as a catalyst. A glass petri dish was put on top of the beaker to reduce solvent evaporation. The system was left to react under stirring at 400 rpm for 1 h at room temperature. The molar ratios used are reported in **Table 4**.

Before coating, silica-soda-lime glass slides were placed in a 250 mL beaker filled with 175 mL of deionized water and a few drops of high pH detergent (LABWASH Premium USB 13, VWR). The slides were then thoroughly cleaned by placing the beaker in an ultrasonic bath for at least 10 min. Then, the same procedure was repeated with MilliQ water and then with absolute ethanol. A final rinsing step with IsoPrOH was applied before allowing the samples to dry under laboratory conditions.

Film Deposition: Silica thin films were deposited using a dip coating technique at ambient temperature (T = 25–30 °C) and laboratory humidity (RH = 35–55%) with a commercial device (Nadetech Innovations ND-DC) at a withdrawal rate of 75 mm min^{-1}. The immersion rates were maintained the same as the withdrawal rates, and a dwelling time of 5 s was applied for all depositions. The films were left to dry in a vertical position overnight.

Artificial Ageing Tests: The efficiency toward atmospheric alteration was evaluated through artificial ageing tests. The protocol consisted of cycling the relative humidity between 90% and 10% every 48 h over a period of 22 days, at a constant temperature of 70 °C.

To do that, glass slides were positioned vertically on a perforated ceramic disc in the centre of a glass desiccator, secured with coated tempered steel paper clamps. Relative humidity was varied between 90% and 10% by respectively adding and removing MilliQ water from the bottom of the desiccator. The temperature was controlled by placing the desiccator inside an oven. Humidity and temperature were regularly monitored using a digital thermometer and hygrometer with an external probe.

Characterization—Surface Profilometry: The thickness of the coating was evaluated with a mechanical, stylus-based surface profiler (KLA-Tencor AlphaStep 500). A step was created between the surface of the film and the substrate by masking a portion of the glass slide with duct tape. After deposition, the tape was removed, and the underlying glass surface was cleaned by gently rubbing with a low-lint wipe (Kimtech Science) soaked in Ethanol. At least three line scans at different positions were performed to measure the step height; the average was calculated as the best estimate. To prevent any possible damage or scratch to the coating, a stylus force lower than 7 mg was applied.

Characterization—UV–Vis Spectroscopy: The optical reflectance of the coatings was evaluated with a portable spectrophotometer (Konica Minolta CM-700d). The instrument uses a diffused illumination integrating sphere system with a powdered barium sulphate ($BaSO_4$) coating and a di:8°/de:8° optical geometry that illuminates the specimen diffusely and detects the light at 8 degrees to the normal line (acceptance angle of 5°).

Spectral reflectance data were acquired in both "specular component excluded" (SCE) and "specular component included" (SCI) mode, using a 10° supplementary standard observer and a circle illumination area of 16 mm in diameter. The wavelength range of acquisition is between 400 and 700 nm, and the spectral resolution is 10 nm. A D65 CIE standard illuminant representing the average daylight was used. This light source has a correlated color temperature of ≈6500 K. To avoid edge effects, the centre of the sample was placed at the reflectance port. A total of three measurements were repeated at the same position, and the average of the measured reflectance data was calculated. The reflectance spectra were enhanced by applying a smoothing function using the Savitzky–Golay algorithm.

The optical transmittance of the coatings was evaluated with a benchtop spectrophotometer (Agilent Cary 100 Series). The instrument has a double-beam optical configuration and a tungsten-halogen lamp as a light source. The spectra were acquired in the wavelength range between 350 and 850 nm. The measurements were performed using an integrating sphere system (Labsphere DRA-CA-30I) with a powdered barium sulphate ($BaSO_4$) coating and a 0°/di geometry, ensuring total transmittance.

Characterization—Infrared Spectroscopy: Chemical structure of the coatings was evaluated with a portable FT-IR spectrometer (Bruker Alpha II), in attenuated total reflectance (ATR) and specular reflectance (SR) configurations. For each spectrum, collected in the wavenumber range between 400 and 4000 cm^{-1}, 128 scans with a spectral resolution of 4 cm^{-1} were recorded. For the SR-IR, a gold mirror was used as a standard reference for all measurements, while for the ATR-IR, air was used as a background. For low absorbance bands, the clarity of the peaks initially obscured by noise was improved by applying smoothing to the spectra using the Savitzky–Golay algorithm.

Characterization—X-Ray Photoelectron Spectroscopy: X-ray photoelectron spectroscopy (XPS) analyses were performed on the coated and uncoated glass samples with an ESCALAB QXi spectrometer (Thermo Fischer, Waltham, MA, USA), employing a monochromatic Al Kα source (15 kV, 20 mA) and a charge compensation gun, needed for correcting the surface charging in case of insulating materials. Survey spectra were acquired at a pass energy of 100 eV, 0.5 eV/step and a dwell time of 50 ms/step. Detailed spectra were recorded at 20 eV pass energy, 0.1 eV/step and dwell time 25 ms/step. The area analyzed was 0.9 mm in linear size. Charge compensation and calibration of the binding energy scale were done, considering the first step the typical BE of O1s band in silicate glass, falling at 532.7 eV[24] because oxygen, as an anion, is less sensible to chemical shifts. The consistency of the charge compensation was tested, considering also the position of the Si2p band (falling ≈103.3 eV in silicate glasses), as well as the position of the C1s for the adventitious (hydro)carbon contamination layer (falling ≈285.0 eV). Deconvolution of the components in the XPS signal was performed with Avantage software. Elemental quantification was carried out by the integration of Si2p, O1s, C1s, Na1s, and Ca2p photoelectron bands, after Shirley-type background subtraction.

Characterization—Atomic Force Microscopy: Morphological properties and mechanical properties of the coatings were evaluated with an atomic force microscope (Bruker Dimension Icon AFM) in PeakForce Tapping (PFT) mode. This technique works by intermittently contacting the sample in a nonresonant mode, effectively combining the advantages of both

Table 5. Poisson's ratio values recommended by Bruker according to the elastic modulus range.

E_S	ν_S
$E_S \leq 100$ MPa	0.5
0.1 GPa $< E_S \leq 1$ GPa	0.4
1 GPa $< E_S \leq 10$ GPa	0.3

contact and TappingMode imaging. It mitigates the damaging lateral forces associated with contact mode and avoids the filtering effect and dynamics of the resonating system typical of TappingMode.

The measurements were conducted under ambient conditions at room temperature with the microscope covered with an acoustic hood to minimize vibrational noise. Monolithic silicon AFM probes (Tap300Al-G, Budget Sensors) were used to characterize the morphology and the mechanical properties of the film at the nanometric scale. The deflection sensitivity was measured on a sapphire surface, the spring constant was calibrated by using the Sader method, and the tip radius was evaluated by the relative method on Bruker's polystyrene test sample. The AFM probe cantilever was vertically oscillated at 1 kHz, which is far from its resonance frequency and helps to avoid the filtering effect. The peak-force amplitude was set to 30 nm and a peak force set point of 15 nN was applied. A scanning rate of 0.601 Hz was used, and the force-distance curves were captured each time the AFM tip tapped on the sample surface, that is, at each pixel (image resolution = 256 px × 256 px). For every experiment, at least three measurements on three different areas were done. The Young's modulus was calculated by fitting part of the unloading curve using the Derjaguin–Muller–Toporov (DMT) model in Equation (2):

$$F - F_{adh} = \frac{4}{3} E^* \sqrt{R(d - d_0)^3} \tag{2}$$

where $F - F_{adh}$ is the force on the cantilever relative to the adhesion force, E^* is the reduced modulus, R is the tip end radius, and $d - d_0$ is the deformation of the sample.

The result of the fit is the reduced modulus E^*, which is related to the Young's modulus of the sample by Equation (3):

$$E^* = \left[\frac{1 - \nu_s^2}{E_s} + \frac{1 + \nu_{tip}^2}{E_{tip}} \right]^{-1} \tag{3}$$

where ν_s and E_s are the Poisson's ratio and the modulus of the sample; ν_{tip} and E_{tip} are the Poisson's ratio and the modulus of the tip. The value of ν_s is set according to recommended values from Bruker, as reported in **Table 5**.

Characterization—Optical Microscopy: The surface appearance was characterized with an optical microscope (Olympus BX43) coupled with a 3.1 megapixel digital color camera (Olympus LC30). Image acquisition was realized through the CellSens entry software. For transmitted bright-field microscopy, the samples were illuminated from below with a high color rendering white LED and the light transmitted through the sample was collected by the objective lens above the sample stage. This configuration was used to observe the overall morphology and any potential inclusions or defects. For reflected darkfield microscopy, the samples were illuminated with a white light fluorescence illumination system (pE-300 white CoolLED) with individual control of three excitation channels covering the UV–vis, blue and green–yellow–red regions. The direct light is blocked by an opaque stop so that an outer ring of illumination "strikes" the sample from above at highly oblique angles. This setup enhances the contrast of surface features by collecting only the light scattered by the sample, effectively highlighting surface textures and any topographical variations.

Supporting Information

Supporting Information is available from the Wiley Online Library or from the author.

Acknowledgements

This work was partially funded by the European Union's Horizon Europe research and innovation action under the grant agreement No. 101060768 (GoGreen project).

Conflict of Interest

The authors declare no conflict of interest.

Data Availability Statement

The data that support the findings of this study are available in the supplementary material of this article.

Keywords

antifouling glass coatings, hybrid silica coatings, inorganic silica coatings, sol–gel synthesis, thin films

Received: January 21, 2025
Revised: March 31, 2025
Published online:

[1] R. Zanini, G. Franceschin, E. Cattaruzza, A. Traviglia, *npj Mater. Degrad.* **2023**, *7*, 38.
[2] G. Schottner, *Chem. Mater.* **2001**, *13*, 3422.
[3] L. Armelao, R. Bertoncello, S. Coronaro, A. Glisenti, *Sci., Technol. Cultural Heritage* **1998** , *1*, 41.
[4] R. Bertoncello, C. Bortolussi, M. Cecchin, D. Lattanzi, Science and Technology for the Safeguard of Cultural Heritage in the Mediterranean Basin, F. Angelo, **2014**, https://www.research.unipd.it/handle/11577/2828946.
[5] B. Dal Bianco, R. Bertoncello, A. Bouquillon, J.-C. Dran, L. Milanese, S. Roehrs, C. Sada, J. Salomon, S. Voltolina, *J. Non-Cryst. Solids* **2008**, *354*, 2983.
[6] R. Bertoncello, L. Milanese, J. C. Dran, A. Bouquillon, C. Sada, *J. Non-Cryst. Solids* **2006**, *352*, 315.
[7] J. D. Mackenzie, E. P. Bescher, *J. Sol–Gel Sci. Technol.* **1998**, *13*, 371.
[8] https://www.siltea.eu/il-restauro-della-grande-vetrata-di-santi-giovanni-e-paolo/.
[9] N. Carmona, M. A. Villegas, J. M. Fernández Navarro, *Thin Solid Films* **2004**, *458*, 121.
[10] M. Monti, B. Dal Bianco, R. Bertoncello, S. Voltolina, *J. Cultural Heritage* **2008**, *9*, 143.
[11] R. Bertoncello, M. Monti, C. Sada, **2016**, *7*, 106, https://doi.org/10.5251/ajsir.2016.7.4.106.113.
[12] L. B. Capeletti, I. M. Baibich, I. S. Butler, J. H. Z. dos Santos, *Spectrochim. Acta, Part A* **2014**, *133*, 619.
[13] V. Purcar, V. Rădiţoiu, A. Rădiţoiu, R. Manea, F. M. Raduly, G. C. Ispas, A. N. Frone, C. A. Nicolae, R. A. Gabor, M. Anastasescu, H. Stroescu, S. Căprărescu, *Coatings* **2021**, *11*, 11.
[14] C. Colleoni, E. Guido, V. Migani, G. Rosace, *J. Industrial Textiles* **2015**, *44*, 815.

[15] V. Rădiţoiu, V. Purcar, A. Rădiţoiu, M. F. Raduly, A. N. Frone, M. Anastasescu, M. Stoica, E. Alexandrescu, R. Şomoghi, R. Manea, G. C. Ispas, L. E. Wagner, S. Căprărescu, *J. Coat. Technol. Res.* **2020**, *17*, 1389.
[16] P. Innocenzi, in *The Sol-to-Gel Transition*, Springer, Berlin, Heidelberg **2019**.
[17] U. Schubert, in *The Sol–Gel Handbook*, John Wiley & Sons, Ltd, Hoboken **2015**, pp. 1–28.
[18] U. (Ulrich) Schubert, in *Synthesis of Inorganic Materials*, Wiley-VCH, New York **2000** .
[19] P. Innocenzi, in *S H Aerogels*, (Eds.: M. A. Aegerter, N. Leventis, M. Koebel, S. A. Steiner III), Springer International Publishing, Cham **2023**, pp. 53–69.
[20] A. G. Xyla, P. G. Koutsoukos, *J. Chem. Soc., Faraday Trans. 1* **1989**, *85*, 3165.
[21] F. A. Andersen, L. Brečević, G. Beuter, D. B. Dell'Amico, F. Calderazzo, N. J. Bjerrum, A. E. Underhill, *Acta Chem. Scand.* **1991**, *45*, 1018.
[22] K. M. Davis, M. Tomozawa, *J. Non-Cryst. Solids* **1996**, *201*, 177.
[23] J. Luo, S. Amma, L. Chen, D. Ngo, J. C. Mauro, C. G. Pantano, S. H. Kim, *J. Non-Cryst. Solids* **2019**, *510*, 179.
[24] NIST X-ray Photoelectron Spectroscopy Database, NIST Standard Reference Database Number 20, National Institute of Standards and Technology, Gaithersburg MD **2023** 20899, https://dx.doi.org/10.18434/T4T88K.
[25] L. H. Grey, H.-Y. Nie, M. C. Biesinger, *Appl. Surf. Sci.* **2024**, *653*, 159319.
[26] H. Imai, H. Hirashima, K. Awazu, *Thin Solid Films* **1999**, *351*, 91.
[27] R. Ghisleni, L. Shao, D. A. Lucca, V. Doan, M. Nastasi, J. Dong, A. Mehner, *Phys. Res. Section B: Beam Interact. Mater. Atoms* **2007**, *261*, 708.
[28] J. Ballarre, D. A. López, A. L. Cavalieri, *Thin Solid Films* **2008**, *516*, 1082.
[29] V. Purcar, O. Cinteza, M. Ghiurea, A. Balan, S. Caprarescu, D. Donescu, *Bull. Mater. Sci.* **2014**, *37*, 107.
[30] V. Purcar, I. Stamatin, O. Cinteza, C. Petcu, V. Raditoiu, M. Ghiurea, T. Miclaus, A. Andronie, *Surf. Coat. Technol.* **2012**, *206*, 4449.
[31] J. Kusz, C. Boissiere, D. Ihiawakrim, O. Ersen, C. Sanchez, S. Parola, *Chem. Mater.* **2023**, *35*, 7671.
[32] A. Walcarius, C. Delacôte, *Chem. Mater.* **2003**, *15*, 4181.
[33] V. G. Parale, D. B. Mahadik, S. A. Mahadik, M. S. Kavale, P. B. Wagh, S. C. Gupta, A. V. Rao, *Ceram. Int.* **2013**, *39*, 835.
[34] M. Pagliaro, R. Ciriminna, G. Palmisano, *J. Mater. Chem.* **2009**, *19*, 3116.
[35] C. Pereira, C. Alves, A. Monteiro, C. Magén, A. M. Pereira, A. Ibarra, M. R. Ibarra, P. B. Tavares, J. P. Araújo, G. Blanco, J. M. Pintado, A. P. Carvalho, J. Pires, M. F. R. Pereira, C. Freire, *ACS Appl. Mater. Interfaces* **2011**, *3*, 2289.
[36] M. Ghodrati, M. Mousavi-Kamazani, Z. Bahrami, *Sci. Rep.* **2023**, *13*, 548.
[37] A. Darmawan, D. L. Handayani, R. E. Saputra, *Appl. Phys. A* **2021**, *127*, 649.